metals

MDPI

Article

A Two-Scale Texture Modelling of AA1050 Aluminum Alloy after Accumulative Roll-Bonding (ARB)

Lisha Shi [1], Shunjie Yao [1], Chen Yuan [1], Haibiao Tu [1] and Hui Wang [1,2,*]

[1] School of Mechanical Engineering, Nantong University, Nantong 226019, China
[2] Institute for Industrial Science, The University of Tokyo, Chiba 153-8505, Japan
* Correspondence: hui_wang@metall.t.u-tokyo.ac.jp or hw737ntu@163.com

Abstract: Texture evolution during accumulative roll-bonding (ARB) is complicated because of the change in the through-thickness position that results from repeated cutting–stacking and roll-bonding. In this study, a macro–micro two-scale modeling was carried out to investigate the behaviors of texture evolution during ARB. The finite element method (FEM) was used to predict the strain history at a macro-scale, while a crystal plasticity FEM was used to reproduce the texture at a micro-scale. The texture evolution along three different cutting–stacking paths was traced and investigated. The patterns of texture transition between the rolling-type, shear-type, and random-type textures were studied by using area fractions of texture components, the distribution of textures, and the distribution of crystal rotation angles.

Keywords: accumulative roll-bonding; FEM; CPFEM; texture evolution

Citation: Shi, L.; Yao, S.; Yuan, C.; Tu, H.; Wang, H. A Two-Scale Texture Modelling of AA1050 Aluminum Alloy after Accumulative Roll-Bonding (ARB). *Metals* **2024**, *14*, 1029. https://doi.org/10.3390/met14091029

Academic Editor: Talal Al-Samman

Received: 19 July 2024
Revised: 19 August 2024
Accepted: 6 September 2024
Published: 10 September 2024

1. Introduction

One of the most effective processing methods to fabricate ultrafine-grained metals is accumulative roll-bonding (ARB) [1–7]. In ARB processes, two sheets are stacked after surface treatment, and then roll-bonding is applied. The roll-bonded sheet is cut into two parts prior to the subsequent cycle. The four steps (surface treatment, stacking, roll-bonding, and cutting) involved in each cycle can be repeated up to a potentially unlimited number of cycles [8]. This cutting–stacking pattern of ARB results in a characteristic through-thickness strain and, accordingly, textural features.

In each single ARB pass, the imposed shear strain decreases from the surface to the center since ARB is usually performed under unlubricated conditions. The strain along the thickness has been numerically predicted. Inoue et al. [9] used the finite element method (FEM) to quantify the through-thickness shear strain and equivalent strain after one cycle using various friction coefficients, and they also developed another FEM model for three cycles [10]. The FEM-predicted equivalent strain in Refs. [9,10] clearly revealed the pattern of strain accumulation during ARB processing.

Between ARB cycles, the cutting–stacking alters the position along the thickness [7,11,12]. For instance, the surface that underwent high shear deformation in the previous cycle is moved to the center in the next cycle and then subjected to compression deformation [13], and this region is further moved to the quarter in the following cycle. This position change results in a great variation in strain along the thickness after multiple cycles, as numerically simulated by Inoue et al. [10] and Wang et al. [14].

These two factors, the non-uniform distribution of the strain introduced in each ARB cycle and the large variation in the strain along the thickness after multiple ARB cycles, pose a great influence on texture evolution. It has been extensively observed that rolling-type and shear-type textures develop at the center and surface, respectively, after each ARB cycle, and textural transition between these two texture components has been widely reported between ARB cycles [8,11,15–18]. In Ref. [19], the FEM-predicted strain was used to reproduce a through-thickness texture using a mean-field crystal plasticity model, Advanced

Lamel (ALAMEL). The shear-type texture on the surface and the rolling-type texture at the center were reproduced, and textural conversion between them was successfully captured. The texture at the quarter is more like a shear-type texture at lower cycles but a rolling-type texture at higher cycles, which implies there are residual texture components during crystallographic rotation. A multiscale framework for multiple ARB cycles was proposed using a solution mapping scheme [20], into which a mean-field viscoplastic self-consistent (VPSC) was embedded. The through-thickness texture gradient and textural anisotropy were accurately predicted using this framework. This texture modeling method enables the simulation of discontinued processes by alleviating FEM mesh distortion. A full-field crystal plasticity FEM (CPFEM), a more advanced texture modeling method, has been used to predict the texture evolution and transition in ARB-processed single crystals [21]. This study accurately reproduced the electron backscatter diffraction (EBSD) characterized texture by up to nine cycles. Textural component distribution and texture evolution were accurately captured, and associated slip activities were investigated. An important finding in Ref. [21] was that the shear-type texture rapidly changed into a rolling-type texture, while the rolling-type texture gradually evolved into a shear-type texture. The difference in the texture transition rate is related to the change in the thickness position.

Compared to uniform-field and mean-field models, the full-field CPFEM is capable of predicting plastic deformation and texture evolution under complex process conditions [22,23], e.g., through-thickness position changes induced textural transitions in ARB. The CPFEM has been applied to ARB-processed single crystals, but the deformation behaviors and texture evolution in single crystals are strongly related to the starting orientation. In contrast, polycrystals are more statistically stable and representative in investigating the behaviors of texture evolution [24]. However, the patterns of texture transition in polycrystals have still not been well studied using full-field CPFEM.

The main purpose of this report is to statistically investigate how the imposed strain influences texture evolution. CPFEM simulations of polycrystalline aluminum alloy AA1050 were performed to study the texture evolution during ARB processes. The predicted texture was validated by experimental X-ray diffraction (XRD) characterizations. The crystallographic rotation along the three different paths was investigated and discussed.

2. Experiment Procedure and Results

2.1. Material and Experiment

A commercial aluminum alloy AA1050 (Al-0.05Cu-0.4Fe-0.05Mg-0.04Mn-0.25Si-0.03Ti-0.05Zn-0.05V-wt%) was used to avoid the effect of other chemical and phase compositions. The received AA1050 was annealed for 1 h at 450 °C. After annealing, the microstructure and texture were characterized using the electron backscatter diffraction (EBSD) technique on a JEOL JSM-7001F. The EBSD mapping was conducted with a working distance of 15 mm and an accelerating voltage of 15 kV. The step size was 2 μm, and the EBSD scanning was conducted along the whole thickness. The starting material presented equiaxed microstructures (Figure 1), and the starting texture was a typical recrystallization texture, i.e., Cube {0 0 1}<1 0 0> orientation-dominated.

The dimension of the sheet was 1.0 mm × 50.0 mm × 400.0 mm (thickness × width × length), and the longitudinal direction was along the rolling direction. The first step of the ARB was stacking two sheets after their contacting surfaces were cleaned and wire-brushed, and the two stacked sheets were welded at the four corners. A nominal reduction of 50% was applied in the roll-bonding step. The rolled sheets were cut into two parts, wire-brushed, and then stacked in preparation for the next cycle. Roll-bonding was conducted without a lubricant, and the rolls were cleaned with acetone before rolling. ARB was conducted up to three cycles since the microstructure almost reached saturation after this.

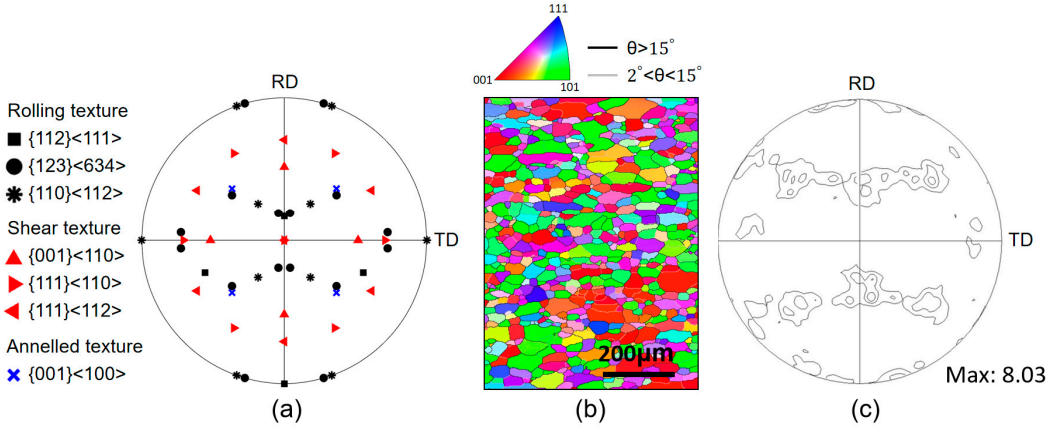

Figure 1. (**a**) Pole figures shows positions of shear-type and rolling-type textures. (**b**) IPF EBSD maps, and (**c**) pole figure of starting material.

The overall bulk texture was measured using the XRD technique. Three incomplete (0~85°) pole figures were obtained, i.e., {1 1 1}, {2 0 0}, and {2 2 0}, using a PANalytical X'Pert-PRO goniometer at 40 kV and 45 mA. The XRD measurements were taken on the RD-TD sections at three positions: the surface, quarter, and center. For the surface region, the XRD measurement was directly performed on the sheet surface. For the quarter and center regions, the ARB-processed sheets were cut into 10 mm × 10 mm and then ground and polished to the corresponding region. Multiple polished sheets were stacked and made for the area to be XRD-measured at 10.0 mm × 10.0 mm. The textures were calculated using ResMat after background correction.

2.2. Experiment Results

In this study, the textural components were divided into three categories: {1 1 2}<1 1 1>, {1 2 3}<6 3 4>, and {1 1 0}<1 1 2> were considered as rolling-type textures, while shear-type texture consisted of {0 0 1}<1 1 0>, {1 1 1}<1 1 2>, and {1 1 1}<1 1 0>. The crystal orientations that belonged to neither the rolling-type textures nor the shear-type textures were called random texture components. The positions of three rolling-type and three shear-type texture components are shown in Figure 1a. Typical rolling-type textures developed at the center after 1-ARB and 3-ARB (Figure 2a), while shear-type textures evolved at the surface (Figure 2c). The texture at the quarter was a shear-type texture after 1-ARB, while it was a rolling-type after 3-ARB (Figure 2b). This kind of texture gradient has been widely observed in ARB-processed aluminum [11,16].

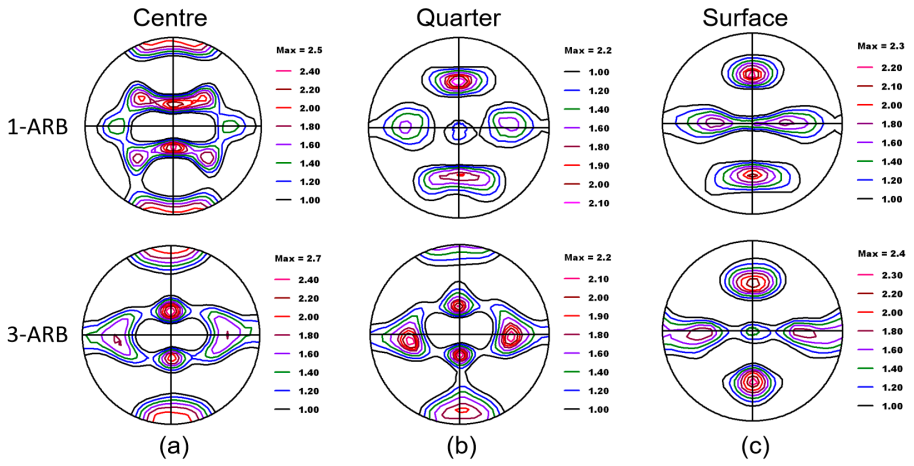

Figure 2. XRD characterized texture at (**a**) center, (**b**) quarter, (**c**) surface after 1-ARB and 3-ARB.

3. Two-Scale Texture Modelling

Figure 3 shows the macro–micro two-scale model. The FEM at the macro-scale was used to predict the through-thickness strain and strain history, while the CPFEM at the micro-scale was utilized to predict the texture as a representative volume element (RVE). The FEM and CPFEM models acted as the globalmodel and submodel, respectively, where the predicted strain history in the FEM model was used to drive the submodel to deformation.

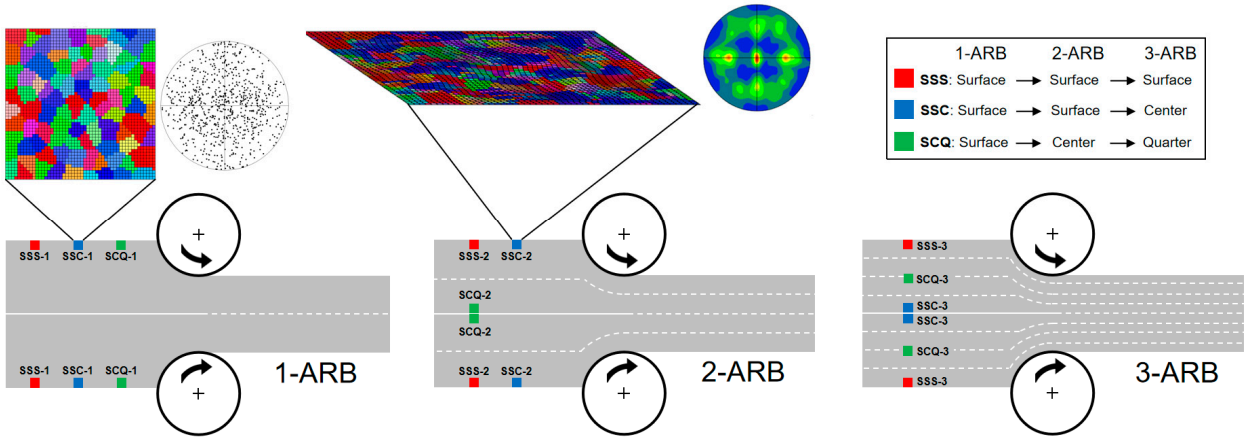

Figure 3. Two-scale model used in this study, FEM at macro-scale and CPFEM at micro-scale.

3.1. Macro-Scale: FEM

At the macro-scale, the FEM was adopted to simulate the whole ARB process (the dark part in Figure 3). The FEM simulation followed the experiment procedure. FEM simulations were performed using the FEM package Abaqus/Standard ver.2018. The FEM model was two-dimensional, and a plain strain deformation condition was assumed. The element size was set as 50 μm × 50 μm after calibrating the mesh resolution. The element type was CPE4R, which was four nodes with one integration point under plane strain conditions. To avoid the hourglassing problem, an enhanced hourglass control was adopted, and this adoption also improved the accuracy of the solution. The elasto-plastic stress–strain curve in the FEM model was obtained from experimental measurements. The FEM model of ARB and the input stress–strain curve are provided in detail in Ref. [14].

3.2. Micro-Scale: CPFEM

At the micro-scale, the full-field CPFEM was adopted to predict the texture evolution in the submodel as RVE. One FEM element (50 μm × 50 μm in dimension), as an RVE, was remeshed into 2500 elements in the CPFEM submodel, and thus, the element size in the CPFEM submodel was 1 μm × 1 μm, comparable to the generally used step size of EBSD scanning. These 2500 elements were grouped into 100 grains. Each element had one initial crystallographic orientation, and the initial orientations of the elements in one grain were the same [25,26]. The crystallographic rotation in different directions enabled the prediction of in-grain subdivisions [22,27]. In Figure 3, the starting texture was randomly distributed in the Euler space, as shown by the {1 1 1} pole figure. The texture after one cycle was reinput as the starting texture of the next cycle, which ensured the continuity of texture evolution during multiple ARB cycles. According to the change in the through-thickness position between cycles, three paths were considered (Figure 3): SSS (surface–surface–surface), SSC (surface–surface–center), and SCQ (surface–center–quarter). For instance, SCQ means the submodel was located at the surface in the first cycle, and it was moved to the center during the second cycle and to the quarter in the third cycle. The deformation of the RVE (submodel) was driven by the strain history of the parent element in the FEM. To achieve statistically stable predictions, each simulation was performed three times using the same settings but different initial orientations, i.e., 7500 elements and 300 grains in total. In the CPFEM model, the hardening model proposed by Bassani was

adopted [28]. This hardening model is a rate-dependent model. The CPFEM theory and implementation, material parameters, and CPFEM modeling of ARB are provided in detail in Ref. [21].

4. Numerical Results

4.1. FEM Prediction of Strain at Macro-Scale

Figure 4a shows the deformed FEM mesh after 1-ARB, and Figure 4b presents the shear strain history at the center, quarter, and surface, as marked by the black squares in Figure 4a. The deformation at the center was compression, as the shear strain is very low in Figure 4b. The FEM mesh was severely sheared at the surface and thus resulted in a high shear strain. In Figure 4b, the increase in the shear strain at ~2.12 s was due to the tilt of the sheet when entering the rolling bite, and the decrease in the shear strain at ~2.20 s was due to the direction change in the relative slide between the sheet and rollers when passing the neutral point.

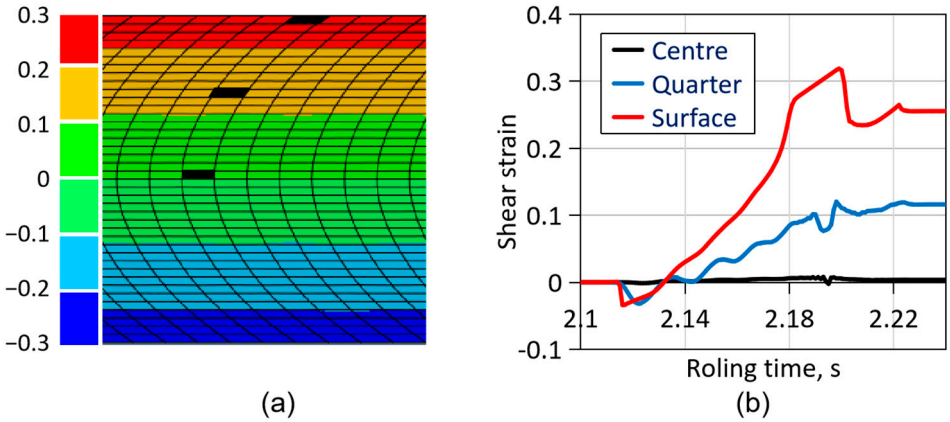

Figure 4. (**a**) Deformed mesh after 1-ARB, and (**b**) history of shear strain at surface, quarter, and center, as marked by the black squares.

The surface position in 1-ARB was moved to either the surface or center in the next cycle. For the surface–surface–surface (SSS) path, the same shear strain as in 1-ARB was imposed in 2-ARB and 3-ARB (Figure 4b). As for the SSC path, the shear-deformed surface in 1-ARB and 2-ARB was moved to the center in 3-ARB and then subjected to compression deformation. The shear strain history along the SCQ path can be similarly deduced.

4.2. CPFEM Prediction of Texture at Micro-Scale

In this section, the texture transition along the three paths (SSS, SSC, SCQ) is presented and compared. The distribution of simulated texture components, {1 1 1} pole figures, area fractions of the rolling texture and shear texture, and the distribution of crystallographic rotation angles were utilized to present the behaviors of texture evolution. It is necessary to note that the simulated texture components after each ARB cycle were plotted on the undeformed FEM mesh for easy display and comparison, e.g., Figure 5a.

4.2.1. Texture Evolution along SSS

Along the SSS path, the region of the submodel was always positioned at the surface (Figure 3). A shear-type texture developed after one cycle (Figure 5a), and its area fraction was 36% (Figure 5b). The shear-type texture was maintained after two and three cycles, and its area fraction increased to 46% and 51%, respectively. A typical shear texture can be observed from the pole figures, and it was similar to the experimental observations shown in Figure 2c. The increases in the shear texture fractions (Figure 5b) during the first cycle were exceedingly fast, and these increases became relatively slow during the second cycle and the third cycle. This means the developed shear texture in the first cycle stayed stable in the second cycle and third cycle along the SSS path. The increasing area fraction of the

shear texture resulted in a higher texture intensity. The growth of the shear texture was at the expense of a random texture. After three cycles, the area fraction of the shear texture was larger than the random texture. The crystal rotation angle in Figure 5c shows a peak at ~20° after one cycle and ~10° after two and three cycles. From Figure 5c, it can be seen that a relatively high fraction of elements possessed large crystal rotation angles in 1-ARB, which indicates the instability of the starting texture, which underwent a large shear deformation. The area fraction of the rolling texture shows a slow growth. This means the presence of the rolling texture was not due to the initially existing rolling texture but evolved during the ARB process, even though this region was located at the surface. Close observation revealed that those rolling textures were almost solely located at the grain boundaries, and this implies that the evolved rolling texture was due to the strong grain interaction, where grain refinement can be clearly seen from the texture component maps in Figure 5a.

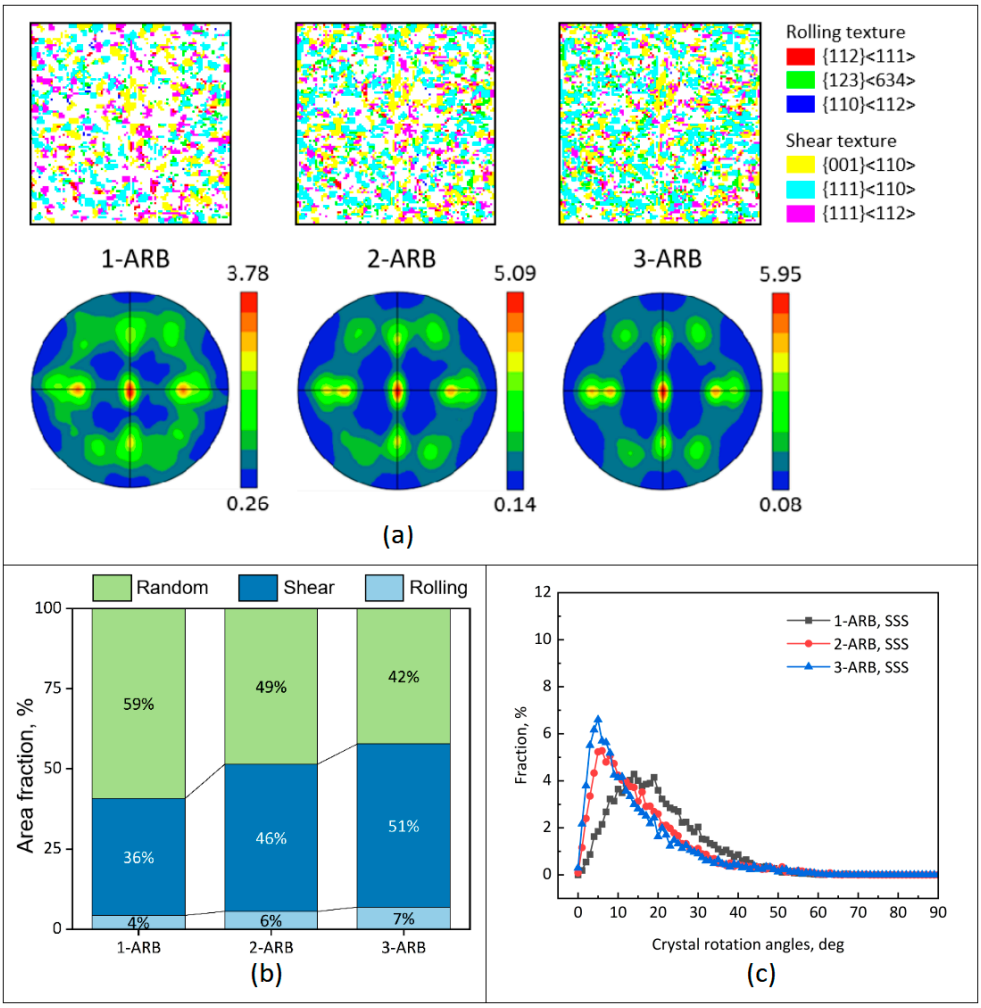

Figure 5. CPFEM predictions of (**a**) texture components and pole figures, (**b**) area fractions of rolling and shear texture, (**c**) distribution of crystal rotation angles along the SSS path.

4.2.2. Texture Evolution along SSC

For the SSC path, the submodel was positioned at the surface in the first and second cycles and was moved to the center in the third cycle. A shear texture developed after the first cycle and intensified after the second cycle (Figure 6a,b). The previously developed shear texture swiftly transitioned into a rolling texture after this region was moved to the center in the third cycle. This textural transition was almost complete, where the area fraction of the shear-type texture became negligible (1%). This fast textural transition implies that the shear texture was exceedingly unstable during compression deformation.

The destruction of the shear texture was almost completely replaced by the formation of the rolling texture (Figure 6b). Among the three rolling-type texture components, the area fractions of {1 1 2}<1 1 1> and {1 2 3}<6 3 4> were obviously higher than {1 1 0}<1 1 2>. The area fraction of the random texture increased slightly in the third cycle. The textural conversion between the shear and rolling texture during the third cycle was quick, as vividly shown by the distribution of crystal rotation angles (Figure 6c), where the distribution of the crystal rotation angles peaked at ~22°, which was even higher than in the first cycle. A quick textural transition has been widely experimentally observed in ARB-process metals.

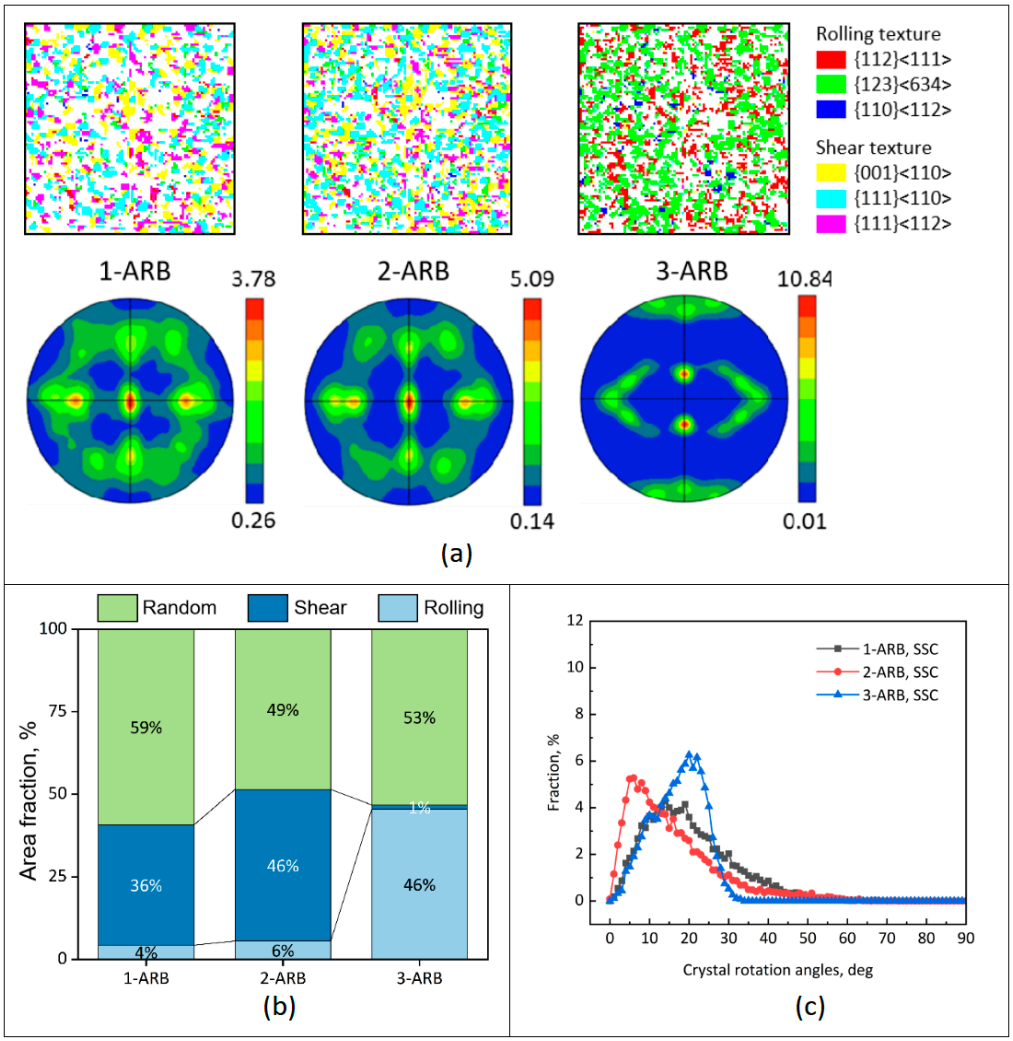

Figure 6. CPFEM predictions of (**a**) texture components and pole figures, (**b**) area fractions of rolling and shear texture, (**c**) distribution of crystal rotation angles along the SSC path.

4.2.3. Texture Evolution along SCQ

As for the SCQ path, the submodel was located at the surface in the first cycle, the center in the second cycle, and the quarter in the third cycle. The shear-type texture developed in the first cycle, and it almost completely transitioned into a rolling-type texture in the second cycle (Figure 7a,b) since the area fraction of the random texture was nearly maintained. The area fraction of the destroyed shear texture was 35% in the second cycle along the SCQ path, while it was 45% in the third cycle along the SSC path. Additionally, the area fraction of the shear texture was negligible. Therefore, this is to say that when the area fraction of the shear texture was higher, the textural transition was fast and complete. The distribution of crystal rotation angles in Figure 7c also confirms the fast textural transition. During the third cycle, a small area fraction of the shear-type texture developed after the

submodel was moved to the quarter region (Figure 7b), while the area fraction of the random texture was reduced in the third cycle. The texture evolution during the third cycle was relatively slow, as shown by the small crystal rotation angles (Figure 7c). The predicted textures at the surface, center, and quarter were consistent with the experimental results (Figure 2), especially in the quarter region.

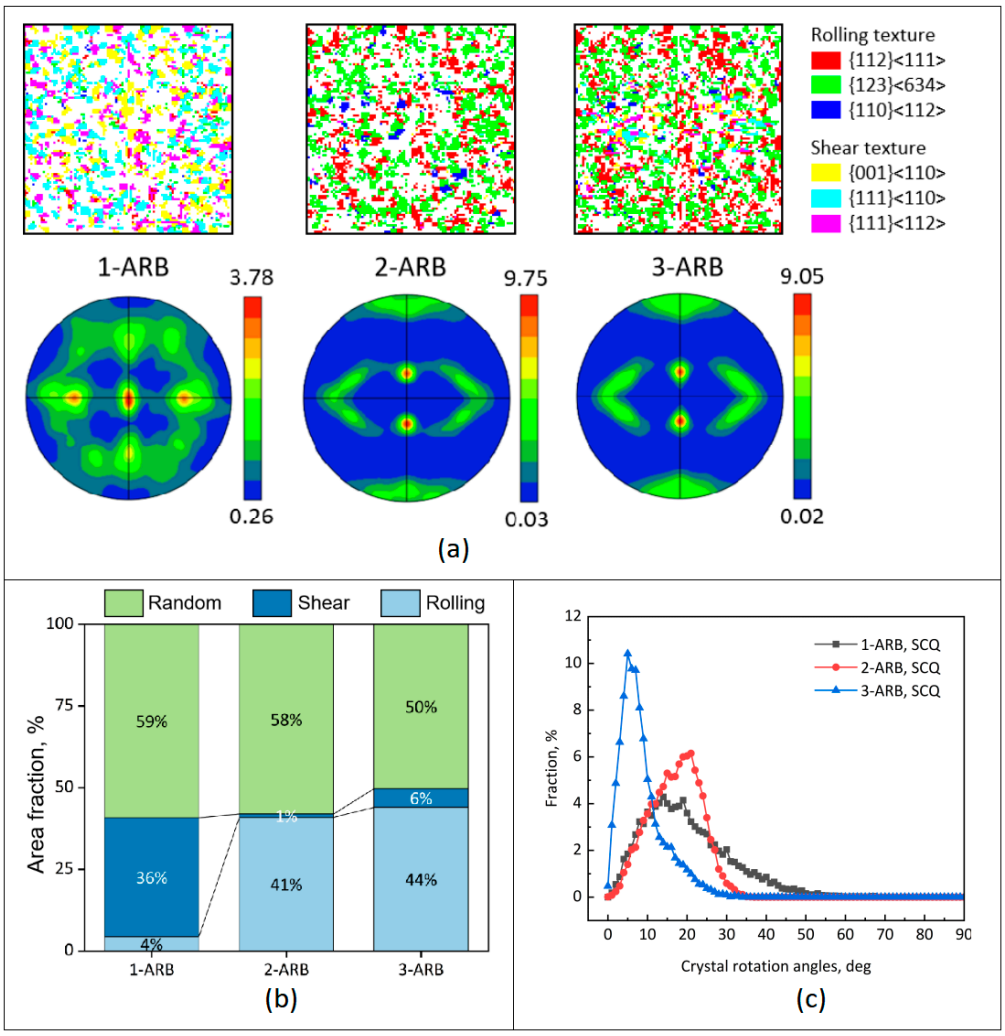

Figure 7. CPFEM predictions of (**a**) texture components and pole figures, (**b**) area fractions of rolling and shear texture, (**c**) distribution of crystal rotation angles along the SCQ path.

5. Discussion

5.1. Brief Comments on the FEM-CPFEM Model

Unlike the uniform-field and mean-field models, the full-field CPFEM has no theoretically assumed homogenization [29,30]. However, an in-element subdivision is beyond the predictability of CPFEM. Increasing the mesh resolution leads to an unaffordable computation time. Meanwhile, a decent number of elements is necessary for a stable statistical study [31]. To improve the balance between the mesh resolution and the required computation resource, CPFEM was applied to three small characteristic regions, RVE, in the current study. The element size in the CPFEM RVE was severely reduced to 1 μm × 1 μm, comparable to the step size of EBSD scanning.

In the CPFEM theory, the plastic strain and crystallographic rotation are completely coupled at each time increment [29]. In this FEM-CPFEM model, the plastic deformation of the elements at the RVE boundaries was driven by the FEM model, while the strain of the inner elements was due to the grain interaction. This explains why this two-scale

FEM-CPFEM model was capable of predicting satisfied textures at three different positions, even after complex strain paths [22].

It is well known that the texture evolution of grain is determined by the intrinsic factor (i.e., crystallographic orientation) and extrinsic factor (i.e., imposed deformation), and these two factors are simultaneously considered in CPFEM [32,33]. The CPFEM predictions show that the shear texture was kept stable when the surface was maintained at the surface since the imposed deformation was the same. In contrast, the formerly evolved shear texture became unstable at the center because of the alteration of the introduced strain. This contrast demonstrates the effect of imposed deformation. The quick and complete textural conversion proves the primary role of the extrinsic factor. The following explains the secondary role of the intrinsic factor in texture evolution. As shown in Figures 2 and 7, the dominant texture component at the quarter region was the shear-type texture after the first cycle, while it was the rolling-type texture after the third cycle. This means the previously developed rolling-type texture at the center in the second cycle was almost preserved at the quarter region in the third cycle. The perseverance of the rolling-type texture at the quarter in the third cycle indicates the influence of initial orientations since the effect of the imposed strain was relatively weak when the region was moved from the center to the quarter.

5.2. Texture Transition during ARB Process

Figures 5–7 clearly reveal the textural transition between the shear-type and rolling-type textures along the three different paths. The developed texture stayed stable if the region was located at the same position along the thickness (e.g., along the SSS path), while the previously evolved texture became unstable if the position was changed (e.g., along the SCQ path). According to the history of shear strain at the surface, quarter, and center (Figure 4), the change in the shear strain resulted in a textural transition. In the following, the behaviors of the texture transition along the SCQ path are discussed. Figure 8 shows the distribution of formed, preserved, and destroyed shear textures and rolling textures during these three cycles, as well as the crystal rotation angles during the texture transition. Figure 9 shows the change in area fraction between shear, rolling, and random textures, as well as the average rotation angles between these textural transitions.

Along the SCQ path, the region was located at the surface in 1-ARB. During 1-ARB, the initially artificially generated rolling texture mainly evolved into a shear texture (Figure 9), while the starting shear texture was primarily preserved, and a large fraction of the random texture changed into a shear texture. The destroyed shear texture (into random and rolling textures) was accomplished by large crystal rotation angles (Figures 8 and 9), similar to the observations in ARB-processed single crystals [21].

The surface region in 1-ARB was moved to the center in 2-ARB (SCQ). During 2-ARB, the destruction of the shear texture was almost complete, which was demonstrated by the change in area fraction (Figure 9); the shear texture was destroyed quickly (Figure 8). The destroyed shear texture (formed in 1-ARB) rotated into a rolling and random texture (Figure 9), and thus, the formation of the rolling texture was also quick. In this ARB cycle, the area fraction of the random texture was further reduced, and the destroyed random texture mainly changed into a rolling texture. The rolling texture was almost preserved (Figure 9) by small rotation angles (Figure 8).

During 3-ARB, the texture transition was mainly between the rolling and random textures (Figure 9) with small rotation angles. The formed shear texture during 3-ARB was mainly from the rolling texture and secondarily from the random texture (Figure 9), and the formation of the shear texture was accompanied by large rotation angles. In contrast, the formation of the rolling texture was relatively slow (Figures 8 and 9), which is consistent with the findings in Ref. [21]. An obvious textural transition between the random and rolling textures was observed though the area fraction of the rolling texture during 3-ARB was almost unchanged, which was unexpected.

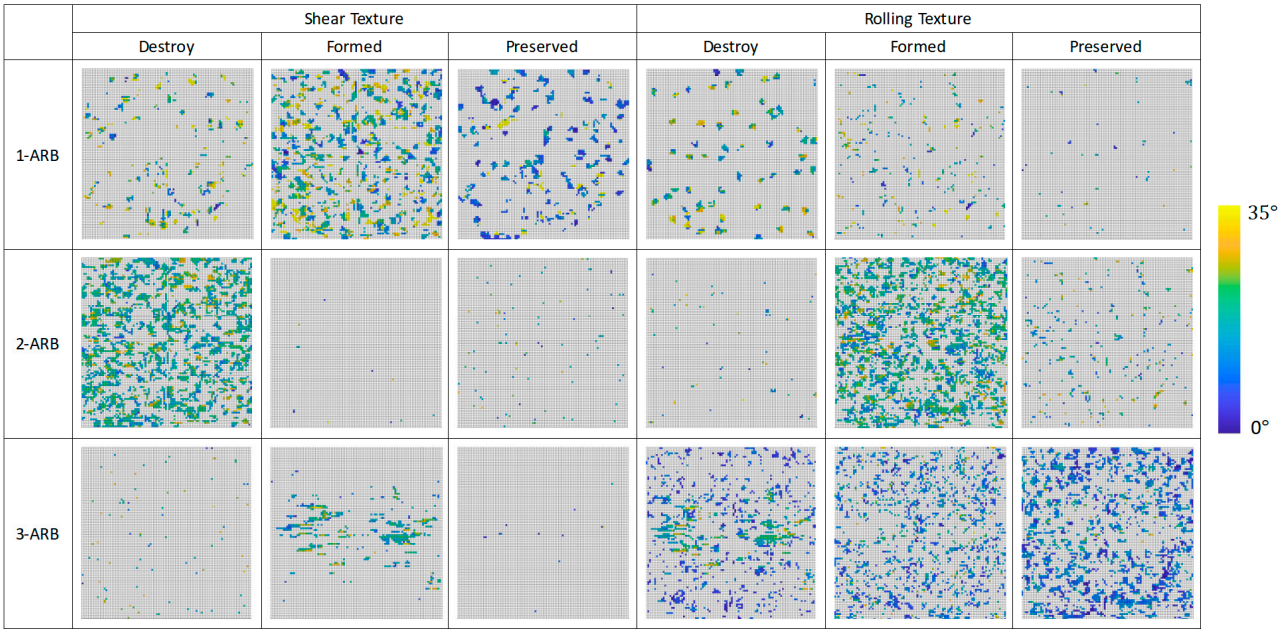

Figure 8. Simulated texture maps show the positions of formed, preserved, and destroyed shear texture and rolling texture along SCQ. The color stands for the crystal rotation angles.

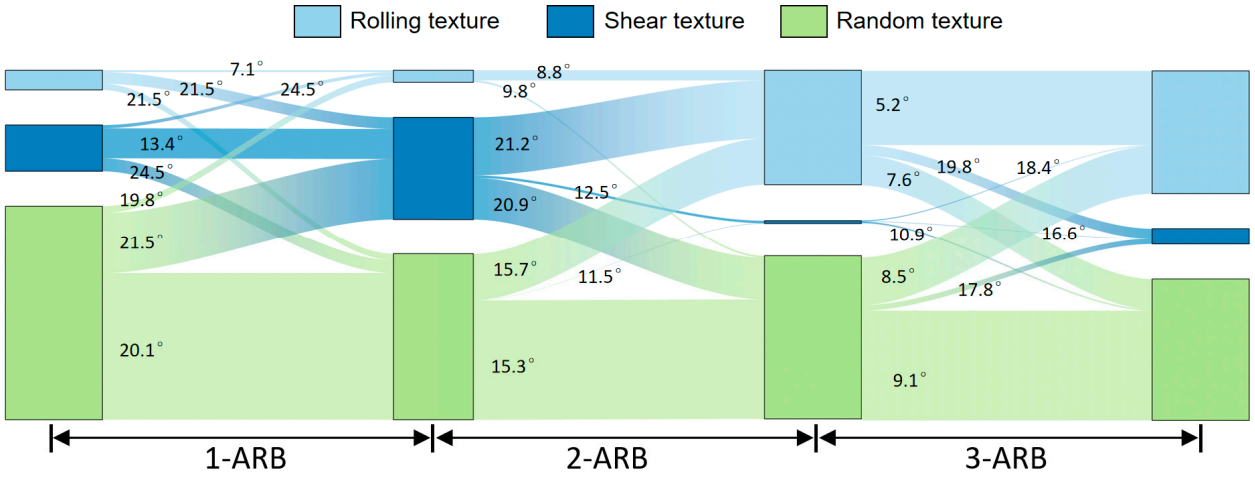

Figure 9. Change in area fraction between shear-texture, rolling-texture, and random-texture along the SCQ path, and the average crystal rotation angles during textural transition.

6. Conclusions

- A two-scale FEM-CPFEM was developed for the texture modeling of ARB processes. The FEM at the macro-scale acted as a globalmodel, and full-field CPFEM at the micro-scale acted as a submodel.
- This FEM-CPFEM modeling method successfully captured the through-thickness (center, quarter, and surface) texture up to three ARB cycles by comparing them with experimentally-XRD-characterized textures.
- Texture evolution along three different paths of the through-thickness position change was predicted. It was found that the texture stayed stable if the through-thickness position was maintained, and it became unstable when the position was changed.
- Textural transition between rolling and random textures was observed (in 3-ARB), even though their area fractions stayed the same, which indicates that the dynamic stability of textures is fractional.

Author Contributions: Conceptualization, H.W.; Methodology, H.W., L.S. and H.T.; Software, L.S., S.Y. and H.T.; Formal analysis, L.S. and C.Y.; Investigation, L.S., S.Y. and C.Y.; Validation, S.Y. and C.Y.; Writing—original draft, L.S., H.T. and H.W.; Writing—review and editing, S.Y. and C.Y.; Supervision, H.W. All authors have read and agreed to the published version of the manuscript.

Funding: This research received no external funding.

Data Availability Statement: The raw data supporting the conclusions of this article will be made available by the authors on request.

Conflicts of Interest: The authors declare no conflict of interest.

References

1. Naseri, M.; Reihanian, M.; Moghaddam, A.O.; Gholami, D.; Hosseini, S.; Alvand, M.; Borhani, E.; Trofimov, E. Improving strength-ductility synergy of nano/ultrafine-structured Al/Brass composite by cross accumulative roll bonding process. *J. Mater. Res. Technol.* **2023**, *26*, 6794–6806. [CrossRef]
2. Sasani, F.; Taheri, A.K.; Pouranvari, M. Correlation between microstructure and mechanical properties of AlMg6/CNT-Al composite produced by accumulative roll bonding process: Experimental and modelling analysis. *Mater. Sci. Eng. A* **2022**, *850*, 143559. [CrossRef]
3. Li, Z.-G.; Li, W.-Q.; Liu, F.-N.; Ma, P.-K.; Liu, P.-L.; Jia, H.-L. Microstructure and mechanical properties of AT31/ATX3105 magnesium alloy composite sheets fabricated by accumulative roll bonding. *J. Mater. Res. Technol.* **2024**, *31*, 1596–1606. [CrossRef]
4. Lei, Z.; Zhang, B.; Zhao, T.; Zhang, Z.; Zhang, Z.; Zhan, S.; Zhao, J.; Wang, K.; Cai, J. Effect of Heat Treatment on the Interfacial Structure and Microstructure of Al/Al/Cu Composites Prepared by Different Accumulative Roll Bonding Passes. *Adv. Eng. Mater.* **2024**, 2400770. [CrossRef]
5. Tayyebi, M.; Alizadeh, M.; Lech, S. Characterizing of a unique Al/Cu FGMMC fabricated via the ARB-CRB process followed by annealing. *J. Alloys Compd.* **2024**, *1000*, 175045. [CrossRef]
6. Zeng, L.; Jiang, P.; Zhang, J.; Zeng, L.; Lu, X. Constructing heterogeneous micro/nano multilayer structure in Al alloys via solute grain boundary segregation for superior strength-ductility synergy. *Mater. Sci. Eng. A* **2024**, *909*, 146810. [CrossRef]
7. Ramkumar, K.R.; Dinaharan, I.; Murugan, N.; Kim, H.S. Development of aluminum matrix composites through accumulative roll bonding: A review. *J. Mater. Sci.* **2024**, *59*, 8606–8649. [CrossRef]
8. Ebrahimi, M.; Wang, Q. Accumulative roll-bonding of aluminum alloys and composites: An overview of properties and performance. *J. Mater. Res. Technol.* **2022**, *19*, 4381–4403. [CrossRef]
9. Inoue, T.; Tsuji, N. Quantification of strain in accumulative roll-bonding under unlubricated condition by finite element analysis. *Comput. Mater. Sci.* **2009**, *46*, 261–266. [CrossRef]
10. Inoue, T.; Yanagida, A.; Yanagimoto, J. Finite element simulation of accumulative roll-bonding process. *Mater. Lett.* **2013**, *106*, 37–40. [CrossRef]
11. Rey-Castañeda, J.E.; Pérez-García, S.A.; García-Pastor, F. Evolution of Through-Thickness Texture and Microstructure of an ARB-Processed Nb1-Zr Alloy. *JOM* **2024**, *76*, 1669–1679. [CrossRef]
12. Chen, R.; Qian, W.; Liu, H.; Xie, W.; Chen, H.; Wang, H.; Yang, B. Dual heterogeneous Cu–Al_2O_3/Cu laminated composite with high strength and ductility prepared by accumulative roll bonding. *J. Mater. Res. Technol.* **2024**, *29*, 3606–3613. [CrossRef]
13. Cantergiani, E.; Riedel, M.; Karhausen, K.F.; Roters, F.; Quadfasel, A.; Falkinger, G.; Engler, O.; Rabindran, R. Simulations of Texture Evolution in the Near-Surface Region During Aluminum Rolling. *Metall. Mater. Trans. A* **2024**, *55*, 3327–3350. [CrossRef]
14. Wang, H.; Su, L.; Yu, H.; Lu, C.; Tieu, A.K.; Liu, Y.; Zhang, J. A new finite element model for multi-cycle accumulative roll-bonding process and experiment verification. *Mater. Sci. Eng. A* **2018**, *726*, 93–101. [CrossRef]
15. Magalhães, D.C.C.; Cintho, O.M.; Rubert, J.B.; Sordi, V.L.; Kliauga, A.M. The role of shear strain during Accumulative Roll-Bonding of multilayered composite sheets: Pattern formation, microstructure and texture evolution. *Mater. Sci. Eng. A* **2020**, *796*, 140055. [CrossRef]
16. Naseri, M.; Alvand, M.; Ahmadi, E.; Hosseini, S.; Gholami, D.; Mourad, A.-H.I.; Borhani, E. Effect of cube texture on local softening of friction stir welded joints for nanostructured AA2024 processed by accumulative roll bonding. *J. Mater. Res. Technol.* **2024**, *28*, 3507–3513. [CrossRef]
17. Dabou, O.; Bensouilah, A.; Baudin, T.; Brisset, F.; Perrière, L.; Helbert, A.-L.; Bradai, D. Evolution of the texture, microstructure, and magnetic properties of a Permimphy alloy after accumulative roll bonding and aging. *J. Mater. Sci.* **2023**, *58*, 15884–15900. [CrossRef]
18. Semenchenko, L.V.; Mier, R.M.; Muyanja, N.S.; Demkowicz, M.J. Near-Surface Layer Perforations as Precursors to Fracture in Accumulative Roll Bonding of a Multilayered Metal Composite. *Metall. Mater. Trans. A* **2024**, *55*, 63–72. [CrossRef]
19. Li, S.; Sun, F.; Li, H. Observation and modeling of the through-thickness texture gradient in commercial-purity aluminum sheets processed by accumulative roll-bonding. *Acta Mater.* **2010**, *58*, 1317–1331. [CrossRef]
20. Prakash, A.; Nöhring, W.G.; Lebensohn, R.A.; Höppel, H.W.; Bitzek, E. A multiscale simulation framework of the accumulative roll bonding process accounting for texture evolution. *Mater. Sci. Eng. A* **2015**, *631*, 104–119. [CrossRef]

21. Wang, H.; Lu, C.; Tieu, K.; Deng, G.; Wei, P.; Liu, Y. A crystal plasticity FEM study of through-thickness deformation and texture in a {112} <111> aluminium single crystal during accumulative roll-bonding. *Sci. Rep.* **2019**, *9*, 3401. [CrossRef]
22. Depriester, D.; Goulmy, J.P.; Barrallier, L. Crystal Plasticity simulations of in situ tensile tests: A two-step inverse method for identification of CP parameters, and assessment of CPFEM capabilities. *Int. J. Plast.* **2023**, *168*, 103695. [CrossRef]
23. Renversade, L.; Quey, R. Intra-grain orientation distributions in deformed aluminium: Synchrotron X-ray diffraction experiment and crystal-plasticity finite-element simulation. *Acta Mater.* **2024**, *262*, 119419. [CrossRef]
24. Abraham, S.T.; Bhat, S.S. Crystal plasticity finite element modelling on the influence of grain size and shape parameters on the tensile stiffness and yield strength. *Mater. Sci. Eng. A* **2023**, *877*, 145155. [CrossRef]
25. Rezaei, M.J.; Sedighi, M.; Pourbashiri, M. Developing a new method to represent the low and high angle grain boundaries by using multi-scale modeling of crystal plasticity. *J. Alloys Compd.* **2023**, *939*, 168844. [CrossRef]
26. Patra, A.; Chaudhary, S.; Pai, N.; Ramgopal, T.; Khandelwal, S.; Rao, A.; McDowell, D.L. ρ-CP: Open source dislocation density based crystal plasticity framework for simulating temperature- and strain rate-dependent deformation. *Comput. Mater. Sci.* **2023**, *224*, 112182. [CrossRef]
27. Shimanek, J.D.; Liu, Z.-K.; Beese, A.M. Effects of misorientation on single crystal plasticity by finite element methods. *Comput. Mater. Sci.* **2024**, *237*, 112879. [CrossRef]
28. Wu, T.; Bassani, J.L.; Laird, C. Latent hardening in single crystals—I. Theory and experiments. *Proc. R. Soc. Lond. A Math. Phys. Sci.* **1997**, *435*, 1–19. [CrossRef]
29. Zhang, X.; Zhao, J.; Kang, G.; Zaiser, M. Geometrically necessary dislocations and related kinematic hardening in gradient grained materials: A nonlocal crystal plasticity study. *Int. J. Plast.* **2023**, *163*, 103553. [CrossRef]
30. Zhou, X.; Zan, S.; Zeng, Y.; Guo, R.; Wang, G.; Wang, T.; Zhao, L.; Chen, M. Comprehensive study of plastic deformation mechanism of polycrystalline copper using crystal plasticity finite element. *J. Mater. Res. Technol.* **2024**, *30*, 9221–9236. [CrossRef]
31. Siddharth, S.; Singh, S.; Kazim, S.M.; Chakraborty, P. Coupled crystal plasticity and damage model for micro crack propagation in polycrystalline microstructures. *Int. J. Fract.* **2024**, *247*, 183–201. [CrossRef]
32. Lakshmanan, A.; Andani, M.T.; Yaghoobi, M.; Allison, J.; Misra, A.; Sundararaghavan, V. A combined experimental and crystal plasticity study of grain size effects in magnesium alloys. *J. Magnes. Alloys* **2023**, *11*, 4445–4467. [CrossRef]
33. Knezevic, M. Crystal plasticity-based finite element simulations of load reversals and hat-shaped draw-bending for predicting the springback behavior of dual-phase steel sheets. *Int. J. Solids Struct.* **2024**, *300*, 112924. [CrossRef]